



The Entire Landslide Velocity

Shiva P. Pudasaini

Technical University of Munich, School of Engineering and Design

Chair of Landslide Research

Arcisstrasse 21, D-80333, Munich, Germany

E-mail: shiva.pudasaini@tum.de

Abstract: The enormous destructive energy carried by a landslide is principally determined by its velocity. Pudasaini and Krautblatter (2022) presented a simple, physics-based analytical landslide velocity model that simultaneously incorporates the internal deformation and externally applied forces. They also constructed various general exact solutions for the landslide velocity. However, previous solutions are incomplete as they only apply to accelerating motions. Here, I advance further by constructing several new general analytical solutions for decelerating motions and unify these with the existing solutions for the landslide velocity. This provides the complete and honest picture of the landslide in multiple segments with accelerating and decelerating movements covering its release, motion through the track, the run-out as well as deposition. My analytical procedure connects several accelerating and decelerating segments by a junction with a kink to construct a multi-sectoral unified velocity solution down the entire path. Analytical solutions reveal essentially different novel mechanisms and processes of acceleration, deceleration and the mass halting. I show that there are fundamental differences between the landslide release, acceleration, deceleration and deposition in space and time as the dramatic transition takes place while the motion changes from the driving force dominated to resisting force dominated sector. I uniquely determine the landslide position and time as it switches from accelerating to decelerating state. Considering all the accelerating and decelerating motions, I analytically obtain the exact total travel time and the travel distance for the whole motion. Different initial landslide velocities with ascending or descending fronts result in strikingly contrasting travel distances, and elongated or contracted deposition lengths. Time and space evolution of the marching landslide with initial velocity distribution consisting of multiple peaks and troughs of variable strengths and extents lead to a spectacular propagation pattern with different stretchings and contractings resulting in multiple waves, foldings, crests and settlements. The analytical method manifests that, computationally costly numerical solutions may now be replaced by a highly cost-effective, unified and complete analytical solution down the entire track. This offers a great technical advantage for the geomorphologists, landslide practitioners and engineers as it provides immediate and very simple solution to the complex landslide motion.

1 Introduction

The dynamics of a landslide are primarily controlled by its velocity which plays a key role for the assessment of landslide hazards, design of protective structures, mitigation measures and landuse planning (Johannesson et al., 2009; Faug, 2010; Dowling and Santi, 2014). Thus, a proper and full understanding of landslide velocity is a crucial requirement for an appropriate modelling of landslide impact force because the associated hazard is directly related to the landslide velocity (Evans et al., 2009; Dietrich and Krautblatter, 2019). However, the mechanical controls of the evolving velocity, runout and impact energy of the landslide have not yet been fully understood.

On the one hand, the available data on landslide dynamics are insufficient while on the other hand, the proper understanding and interpretation of the data obtained from field measurements are often challenging. This is because of the very limited information of the boundary conditions and the material properties. Moreover, dynamic field data are rare and after event static data are often only available for single locations (de Haas et al., 2020). So, much of the low resolution measurements are locally or discretely based on points in time and space (Berger et al., 2011; Theule et al., 2015; Dietrich and Krautblatter, 2019). This is the reason for why laboratory or field experiments (Iverson and Ouyang, 2015; de Haas and van Woerkom, 2016; Pilvar et



46 al., 2019; Baselt et al., 2021) and theoretical modelling (Le and Pitman, 2009; Pudasaini, 2012; Pudasaini and
47 Mergili, 2019) remain the major solutions of the problems associated with the mass flow dynamics. Several
48 comprehensive numerical modelling for mass transports are available (McDougall and Hungr, 2005; Frank et
49 al., 2015; Iverson and Ouyang, 2015; Cuomo et al., 2016; Mergili et al., 2020; Liu et al. 2021). Yet, numer-
50 ical simulations are approximations of the physical-mathematical model equations and their validity is often
51 evaluated empirically (Mergili et al., 2020). In contrast, exact, analytical solutions can provide better insights
52 into complex flow behaviors (Faug et al., 2010; Gauer, 2018; Pudasaini and Krautblatter, 2021,2022; Faraoni,
53 2022). Furthermore, analytical and exact solutions to non-linear model equations are necessary to elevate the
54 accuracy of numerical solution methods based on complex numerical schemes (Chalfen and Niemiec, 1986;
55 Pudasaini, 2016). This is very useful to interpret complicated simulations and/or avoid mistakes associated
56 with numerical simulations. However, the numerical solutions (Mergili et al., 2020; Shugar et al., 2021) can
57 cover the broad spectrum of complex flow dynamics described by advanced mass flow models (Pudasaini and
58 Mergili, 2019), and once tested and validated against the analytical solutions, may provide even more accurate
59 results than the simplified analytical solutions (Pudasaini and Krautblatter, 2022).

60 Since Voellmy's pioneering work, several analytical models and their solutions have been presented for mass
61 movements including landslides, avalanches and debris flows (Voellmy, 1955; Salm, 1966; Perla et al., 1980;
62 McClung, 1983). However, on the one hand, all of these solutions are effectively simplified to the mass point
63 or center of mass motion. None of the existing analytical velocity models consider advection or internal defor-
64 mation. On the other hand, the parameters involved in those models only represent restricted physics of the
65 landslide material and motion. Pudasaini and Krautblatter (2022) overcame those deficiencies by introducing a
66 simple, physics-based general analytical landslide velocity model that simultaneously incorporates the internal
67 deformation and externally applied forces, consisting of the net driving force and the viscous resistant. They
68 showed that the non-linear advection and external forcing fundamentally regulate the state of motion and
69 deformation. Since analytical solutions provide the fastest, the most cost-effective and best rigorous answer
70 to the problem, they constructed several general exact analytical solutions. Those solutions cover the wider
71 spectrum of landslide velocity and directly reduce to the mass point motion as their solutions bridge the gap
72 between the negligibly deforming and geometrically massively deforming landslides. They revealed the fact
73 that shifting, up-lifting and stretching of the velocity field stem from the forcing and non-linear advection. The
74 intrinsic mechanism of their solution described the breaking wave and emergence of landslide folding. This
75 demonstrated that landslide dynamics are architected by advection and reigned by the system forcing.

76 However, the landslide velocity solutions presented by Pudasaini and Krautblatter (2022) are only applicable
77 for the accelerating motions associated with the positive net driving forces, and thus are incomplete. Here, I
78 extend their solutions that cover the entire range of motion, from initiation to acceleration, to deceleration to
79 deposition as the landslide mass comes to a halt. This includes both the motions with positive and negative
80 net driving forces. This constitutes a unified foundation of landslide velocity in solving technical problems.
81 As exact, analytical solutions disclose many new and essential physics of the landslide release, acceleration,
82 deceleration and deposition processes, the solutions derived in this paper may find applications in geomorpho-
83 logical, environmental, engineering and industrial mass transports down entire slopes and channels in quickly
84 and adequately describing the entire flow dynamics, including the flow regime changes.

85 2 The Model

86 For simplicity, I consider a geometrically two-dimensional motion down a slope. Let t be time, (x, z) be the
87 coordinates and (g^x, g^z) the gravity accelerations along and perpendicular to the slope, respectively. Let, h
88 and u be the flow depth and the mean flow velocity of the landslide along the slope. Similarly, γ, α_s, μ be
89 the density ratio between the fluid and the solid particles ($\gamma = \rho_f / \rho_s$), volume fraction of the solid particles
90 (coarse and fine solid particles), and the basal friction coefficient ($\mu = \tan \delta$), where δ is the basal friction angle
91 of the solid particles, in the mixture material. Furthermore, K is the earth pressure coefficient (Pudasaini and
92 Hutter, 2007), and β is the viscous drag coefficient. By reducing the multi-phase mass flow model (Pudasaini



93 and Mergili, 2019), Pudasaini and Krautblatter (2022) constructed the simple landslide velocity equation:

$$\frac{\partial u}{\partial t} + u \frac{\partial u}{\partial x} = \alpha^a - \beta u^2, \quad (1)$$

94 where α^a and β constitute the net driving and the resisting forces in the system. Moreover, α^a is given by the
95 expression $\alpha^a := g^x - (1 - \gamma)\alpha_s g^z \mu - g^z \{((1 - \gamma)K + \gamma)\alpha_s + (1 - \alpha_s)\} h_g$ (this includes the forces due to gravity,
96 Coulomb friction, lubrication, and liquefaction as well as the surface gradient indicated by h_g), and β is the
97 viscous drag coefficient.

98 Pudasaini and Krautblatter (2022) constructed many exact analytical solutions to the landslide velocity equation
99 (1). However, their solutions were restricted to the physical situation in which the net driving force is
100 positive, i.e., $\alpha^a > 0$. Following the classical method by Voellmy (Voellmy, 1955) and extensions by Salm (1966)
101 and McClung (1983), the velocity model (1) can be amended and used for multiple slope segments to describe
102 the accelerating and decelerating motions as well as the landslide run-out. These are also called the release,
103 track and run-out segments of the landslide, or avalanche (Gubler, 1989). However, for the gentle slope, or
104 the run-out, the frictional force may dominate gravity. In this situation, the sign of α^a in (1) changes. So, to
105 complement the solutions constructed in Pudasaini and Krautblatter (2022), here, I consider (1) with negative
106 net driving force resulting in the decelerating motion, and finally the landslide deposition. For this, I change
107 the sign of α^a and rewrite (1) as:

$$\frac{\partial u}{\partial t} + u \frac{\partial u}{\partial x} = -\alpha_d - \beta u^2. \quad (2)$$

108 Note that a and d in α^a and α_d in (1) and (2) indicate the accelerating (ascending) and decelerating (descending)
109 motions, respectively. We follow these notations for all the models and solutions considered and developed
110 below.

111 The main purpose here is to construct several new analytical solutions to (2), and combine these with the
112 existing solutions (Pudasaini and Krautblatter, 2022) for (1). This facilitates the description of the landslide
113 motion down a slope consisting of multiple segments with accelerating and decelerating movements, with
114 positive and negative net driving forces, as well as the landslide run-out. This will provide us with the
115 complete and unified picture of the landslide motions in different segments- from release to track to run-out
116 and deposition as required by the practitioners.

117 **Terminology and convention:** To avoid any possible ambiguity, I define the terminology for accelerating
118 and decelerating motions and motions with ascending and descending velocities. Consider model (1). Then,
119 we have the following two situations.

120 **Accelerating motion – I:** The landslide accelerates if the total system force $\alpha^a - \beta u^2 > 0$. This happens
121 only if $\alpha^a > 0$, that is, when the net driving force is positive, and the initial velocity u_0 satisfies the condition
122 $u_0 < \sqrt{\alpha^a/\beta}$.

123 **Decelerating motion – II:** The landslide decelerates if $\alpha^a - \beta u^2 < 0$. This can happen in two completely
124 different situations.

125 **II.1 – Weak-deceleration:** First, consider $\alpha^a > 0$, but relatively high initial velocity such that $u_0 > \sqrt{\alpha^a/\beta}$.
126 Then, although the net driving force is positive, due to the high value of the initial velocity than the
127 characteristic limit velocity of the system $\sqrt{\alpha^a/\beta}$, the landslide attains decelerating motions due to the
128 high drag force, and approaches down to $\sqrt{\alpha^a/\beta}$ as the landslide moves. I call this the weak-deceleration.

129 **II.2 – Strong-deceleration:** Second, consider $\alpha^a = -\alpha_d < 0$, which is the state of the negative net driving
130 force associated with the system (2). Then, for any choice of the initial velocity, the landslide must
131 decelerate. I call this the strong-deceleration. The decelerating velocity in **II.2** is always below the
132 decelerating velocity in **II.1**

133 **Ascending and descending motions:** Unless otherwise stated and without loss of generality, I make the
134 following convention. When the net driving force is positive and **I** is satisfied, the accelerating landslide motion



135 (velocity) is also called the ascending motion. Because, in this situation, the motion is associated with the
136 ascending velocity. When the net driving force is negative or **II.2** is satisfied, the decelerating landslide motion
137 (velocity) is also called the descending motion, because for this, the velocity always decreases. I will separately
138 treat **II.1** in Section 5.4.

139 The landslide velocity solutions for **I** and **II.1** are associated with the positive net driving forces, and have
140 been presented in Pudasaini and Krautblatter (2022). Here, I present solutions for **II.2** associated with the
141 negative net driving force and unify them with previous solutions. This completes the construction of simple
142 analytical solutions.

143 3 The Entire Landslide Velocity: Simple Solutions

144 As (2) describes fundamentally different process of landslide motion than (1), for the model (2), all solutions
145 derived by Pudasaini and Krautblatter (2022) must be thoroughly re-visited with the initial condition for veloc-
146 ity of the following segment being that obtained from the lower end of the upstream segment. This way, we can
147 combine solutions to models (1) and (2) to analytically describe the landslide motion for the entire slope, from
148 its release, through the track to the run-out, including the total travel distance and the travel time. This is the
149 novel aspect of this contribution which makes the present solution system complete that the practitioners and
150 engineers can directly apply these solutions to solve their technical problems. However, note that, decelerating
151 motion can be constructed independent of whether or not it follows an accelerating motion. In other situation,
152 accelerating motion could follow the decelerating motion. So, depending on the state of the net driving forces,
153 different scenarios are possible.

154 Because of their increasing and decreasing behaviors, velocity solutions associated with the model (1) is indi-
155 cated by the symbol \nearrow , and that associated with the model (2) it is indicated by the symbol \searrow . These are
156 the ascending and descending motions, respectively. All the solutions indicated by the symbol \searrow are entirely
157 new. By combining these two types of solutions, we obtain the complete solution for the landslide motion, i.e.,
158 ‘the solution \nearrow + the solution \searrow = the complete solution’.

159 3.1 Steady-state motion

160 The steady-state solution describes one of the simplest states of dynamics that are independent of time ($\partial u/\partial t =$
161 0). So, I begin with constructing simple analytical solutions for the steady-state landslide velocity equations,
162 reduced from (1) and (2):

$$u \frac{\partial u}{\partial x} = \alpha^a - \beta u^2, \quad (3)$$

163 and

$$u \frac{\partial u}{\partial x} = -\alpha_d - \beta u^2, \quad (4)$$

164 respectively. Following Pudasaini and Krautblatter (2022), the steady-state solution for (3) takes the form:

$$\nearrow u(x; \alpha^a, \beta) = \sqrt{\frac{\alpha^a}{\beta} \left[1 - \left(1 - \frac{\beta}{\alpha^a} u_0^2 \right) \frac{1}{\exp(2\beta(x - x_0))} \right]}, \quad (5)$$

165 where, $u_0 = u(x_0)$ is the initial velocity at x_0 . Similarly, the steady-state solution for (4) can be constructed,
166 which reads:

$$\searrow u(x; \alpha_d, \beta) = \sqrt{\frac{1}{\beta} [\exp\{-2\beta(x - x_0)\} (\beta u_0^2 + \alpha_d) - \alpha_d]}, \quad (6)$$

167 However, solutions (5) and (6) appear to be structurally similar, and by changing α^a to $-\alpha_d$, (5) can be
168 simplified to yield (6). These solutions describe the dynamics of a landslide (the velocity u) as a function of
169 the downslope position, x , one of the basic dynamic quantities required by engineers and practitioners for the
170 quick assessment of landslide hazards.



171 3.2 Mass point motion

172 Assume no or negligible local deformation (e.g., $\partial u/\partial x \approx 0$), or a Lagrangian description. Both are equivalent
 173 to the mass point motion. In this situation, only the ordinary differentiation with respect to time is involved,
 174 and $\partial u/\partial t$ can be replaced by du/dt . Then, the models (1) and (2) reduce to

$$\frac{du}{dt} = \alpha^a - \beta u^2, \quad (7)$$

175 and

$$\frac{du}{dt} = -\alpha_d - \beta u^2, \quad (8)$$

176 respectively, for the positive and negative net driving forces. Solutions to mass point motions provide us with
 177 quick information of the landslide motion in time. Such solutions are often required and helpful to analyze
 178 the time evolution of primarily largely intact sliding mass without any substantial spatial deformation. So, we
 179 proceed with the solution for the mass point motions.

180 3.2.1 Accelerating landslide

181 Exact analytical solution for (7) can be constructed, providing the velocity for the landslide motion in terms
 182 of a tangent hyperbolic function (Pudasaini and Krautblatter, 2022):

$$\nearrow u(t; \alpha^a, \beta) = \sqrt{\frac{\alpha^a}{\beta}} \tanh \left[\sqrt{\alpha^a \beta} (t - t_0) + \tanh^{-1} \left(\sqrt{\frac{\beta}{\alpha^a}} u_0 \right) \right], \quad (9)$$

183 where, $u_0 = u(t_0)$ is the initial velocity at time $t = t_0$. The mass point solutions also enable us to exactly
 184 obtain the travel time, travel position and distance of the landslide down the slope that I derive below. These
 185 quantities are of direct practical importance.

186 **Travel time for accelerating landslide:** The travel time for the accelerating landslide in any sector of the
 187 flow path can be obtained by using the (maximum) velocity at the right end in that sector, say u_{max} , in (9)

$$\nearrow t_{max} = t_0 + \frac{1}{\sqrt{\alpha^a \beta}} \left[\tanh^{-1} \left(\sqrt{\frac{\beta}{\alpha^a}} u_{max} \right) - \tanh^{-1} \left(\sqrt{\frac{\beta}{\alpha^a}} u_0 \right) \right]. \quad (10)$$

188

189 **The position of accelerating landslide:** Since $u(t) = dx/dt$, (9) can be integrated to obtain the landslide
 190 position as a function of time (Pudasaini and Krautblatter, 2022):

$$\nearrow x(t; \alpha^a, \beta) = x_0 + \frac{1}{\beta} \ln \left[\cosh \left\{ \sqrt{\alpha^a \beta} (t - t_0) - \tanh^{-1} \left(\sqrt{\frac{\beta}{\alpha^a}} u_0 \right) \right\} \right] - \frac{1}{\beta} \ln \left[\cosh \left\{ -\tanh^{-1} \left(\sqrt{\frac{\beta}{\alpha^a}} u_0 \right) \right\} \right], \quad (11)$$

191 where $x_0 = x(t_0)$ corresponds to the position at the initial time t_0 .

192 **The travel distance for accelerating landslide:** The maximum travel distance x_{max} is achieved by setting
 193 $t = t_{max}$ from (10) in to (11), yielding:

$$\nearrow x_{max} = x_0 + \frac{1}{\beta} \ln \left[\cosh \left\{ \sqrt{\alpha^a \beta} (t_{max} - t_0) - \tanh^{-1} \left(\sqrt{\frac{\beta}{\alpha^a}} u_0 \right) \right\} \right] - \frac{1}{\beta} \ln \left[\cosh \left\{ -\tanh^{-1} \left(\sqrt{\frac{\beta}{\alpha^a}} u_0 \right) \right\} \right]. \quad (12)$$

194 Solutions (9)-(12) provide us the velocity of the negligibly deformable (or non-deformable) accelerating landslide
 195 together with its travel time, position and travel distance, supplying us with all necessary information required
 196 to fully describe the state of the landslide motion.



197 3.2.2 Decelerating landslide

198 However, the exact analytical solution for (8), i.e., the velocity of the decelerating landslide, appears to be the
 199 negative of a tangent function:

$$\searrow u(t; \alpha_d, \beta) = -\sqrt{\frac{\alpha_d}{\beta}} \tan \left[\sqrt{\alpha_d \beta} (t - t_0) + \tan^{-1} \left(-\sqrt{\frac{\beta}{\alpha_d}} u_0 \right) \right], \quad (13)$$

200 where, $u_0 = u(t_0)$ is the initial velocity at time $t = t_0$. The solution in (13) is fundamentally different than
 201 the one in (9) for the accelerating landslide. In contrast to (9), which always have upper ($u > \sqrt{\alpha^a/\beta}$) or
 202 lower bound ($u < \sqrt{\alpha^a/\beta}$) (depending on the initial condition), (13) provides only the decreasing (velocity)
 203 solution without any lower bound that must be constrained with the possible (final) velocity in the sector under
 204 consideration, say, u_f , particularly $u_f = 0$, when the landslide comes to a halt.

205 **Travel time for decelerating landslide:** The maximum travel time in the sector under consideration, t_{max} ,
 206 is achieved from (13) by setting the velocity at the right end of this sector, say, u_{min} i.e.,

$$\searrow t_{max} = t_0 + \frac{1}{\sqrt{\alpha_d \beta}} \left[\tan^{-1} \left(-\sqrt{\frac{\beta}{\alpha_d}} u_{min} \right) - \tan^{-1} \left(-\sqrt{\frac{\beta}{\alpha_d}} u_0 \right) \right]. \quad (14)$$

207 The final time the mass comes to a standstill is obtained from (14) by setting $u_{min} = 0$.

208 **The position of decelerating landslide:** Again, by setting the relation $u(t) = dx/dt$, (13) can be integrated
 209 to obtain the landslide position as a function of time:

$$\searrow x(t; \alpha_d, \beta) = x_0 + \frac{1}{\beta} \ln \left[\cos \left\{ \tan^{-1} \left(\sqrt{\frac{\beta}{\alpha_d}} u_0 \right) - \sqrt{\alpha_d \beta} (t - t_0) \right\} \right] - \frac{1}{\beta} \ln \left[\cos \left\{ \tan^{-1} \left(\sqrt{\frac{\beta}{\alpha_d}} u_0 \right) \right\} \right], \quad (15)$$

210 where $x_0 = x(t_0)$ corresponds to the position at the initial time t_0 .

211 **The travel distance for decelerating landslide:** The maximum travel distance x_{max} is achieved by setting
 212 $t = t_{max}$ from (14) in to (15), yielding:

$$\searrow x_{max} = x_0 + \frac{1}{\beta} \ln \left[\cos \left\{ \tan^{-1} \left(\sqrt{\frac{\beta}{\alpha_d}} u_0 \right) - \sqrt{\alpha_d \beta} (t_{max} - t_0) \right\} \right] - \frac{1}{\beta} \ln \left[\cos \left\{ \tan^{-1} \left(\sqrt{\frac{\beta}{\alpha_d}} u_0 \right) \right\} \right]. \quad (16)$$

213 Solutions (13)-(16) supply us with the velocity of practically non-deformable decelerating landslide including its
 214 travel time, position and travel distance. All these information are necessary to fully characterise the landslide
 215 dynamic.

216 **Total time and total travel distance:** It is important to note that the overall total time t_{oa} and the overall
 217 total travel distance x_{oa} must include all the times in ascending (\nearrow) and descending (\searrow) motions until the
 218 mass comes to the halt, where oa stands for the overall motion. Here, ascending and descending motions refer
 219 to the increasing and decreasing landslide velocities in accelerating and decelerating sections of the sliding path.

220 In this section I constructed simple exact analytical solutions for the accelerating and decelerating landslides
 221 when they are governed by simple time-independent (steady-state) or locally non-deformable (mass point)
 222 motions. However, their applicabilities are limited due to their respective constraints of not changing in time
 223 or no internal deformation.

224 4 The Entire Landslide Velocity: General Solutions

225 In reality, the landslide motion can change in time and space. To cope with these situations, we must construct
 226 analytical landslide velocity solutions as functions of time and space. Below, I focus on these important aspects.
 227 These general solutions cover all the simple solutions presented in the previous section as special cases. The
 228 solutions are constructed for both the accelerating and decelerating motions.



229 4.1 Accelerating landslide – general velocity

230 Consider the initial value problem for the accelerating landslide motion (1) with the positive net driving force:

$$\frac{\partial u}{\partial t} + u \frac{\partial u}{\partial x} = \alpha^a - \beta u^2, \quad u(x, 0) = s_0(x). \quad (17)$$

231 This is a non-linear advective–dissipative system, and can be perceived as an inviscid, dissipative, non-
 232 homogeneous Burgers’ equation (Burgers, 1948). Following the mathematical procedure in Montecinos (2015),
 233 Pudasaini and Krautblatter (2022) constructed an exact analytical solution for (17):

$$\nearrow u(x, t) = \sqrt{\frac{\alpha^a}{\beta}} \tanh \left[\sqrt{\alpha^a \beta} t + \tanh^{-1} \left\{ \sqrt{\frac{\beta}{\alpha^a}} s_0(y) \right\} \right], \quad (18)$$

234 where $y = y(x, t)$ is given by

$$\nearrow x = y + \frac{1}{\beta} \ln \left[\cosh \left\{ \sqrt{\alpha^a \beta} t + \tanh^{-1} \left\{ \sqrt{\frac{\beta}{\alpha^a}} s_0(y) \right\} \right\} \right] - \frac{1}{\beta} \ln \left[\cosh \left\{ \tanh^{-1} \left\{ \sqrt{\frac{\beta}{\alpha^a}} s_0(y) \right\} \right\} \right], \quad (19)$$

235 and, $s_0(x) = u(x, 0)$ provides the functional relation for $s_0(y)$. Which is the direct generalization of the mass
 236 point solution given by (9).

237 As in the mass point solutions, (18) and (19) are also primarily expressed in terms of the tangent hyperbolic, and
 238 the composite of logarithm, cosine hyperbolic and tangent hyperbolic functions. However, now, these solutions
 239 contain important new dynamics embedded into solutions through the terms associated with the function $s_0(y)$
 240 describing the spatial variations in addition to the time variations of landslide dynamics. This makes the general
 241 solution system (18) and (19) more complex, but much closer to the reality than simple solutions constructed
 242 in Section 3.2.1 that are applicable either for the time or spatial variations of the landslide velocity.

243 4.2 Decelerating landslide – general velocity

244 Next, consider the initial value problem for the decelerating landslide motion (2) with the negative net driving
 245 force:

$$\frac{\partial u}{\partial t} + u \frac{\partial u}{\partial x} = -\alpha_d - \beta u^2, \quad u(x, 0) = s_0(x). \quad (20)$$

246 This is also a non-linear advective–dissipative system, or an inviscid, dissipative, non-homogeneous Burgers’
 247 equation. Following Pudasaini and Krautblatter (2022) I have constructed an exact analytical solution for (18),
 248 which reads:

$$\searrow u(t; \alpha_d, \beta) = -\sqrt{\frac{\alpha_d}{\beta}} \tan \left[\sqrt{\alpha_d \beta} t + \tan^{-1} \left\{ -\sqrt{\frac{\beta}{\alpha_d}} s_0(y) \right\} \right], \quad (21)$$

249 where $y = y(x, t)$ is given by

$$\searrow x(t; \alpha_d, \beta) = y + \frac{1}{\beta} \ln \left[\cos \left\{ \tan^{-1} \left\{ \sqrt{\frac{\beta}{\alpha_d}} s_0(y) \right\} - \sqrt{\alpha_d \beta} t \right\} \right] - \frac{1}{\beta} \ln \left[\cos \left\{ \tan^{-1} \left\{ \sqrt{\frac{\beta}{\alpha_d}} s_0(y) \right\} \right\} \right], \quad (22)$$

250 and, $s_0(x) = u(x, 0)$ provides the functional relation for $s_0(y)$. Which is the direct generalization of the mass
 251 point solution given by (13).

252 As in the mass point solutions, (21) and (22) are also basically expressed in terms of the tangent, and the
 253 composite of logarithm, cosine and tangent functions. However, these solutions now contain important new
 254 dynamics included into the solutions through the terms associated with the function $s_0(y)$ describing the spatial
 255 variations in addition to the time variations of landslide dynamics. This makes the general solution system
 256 (21) and (22) more complex, but closer to the reality than simple solutions constructed in Section 3.2.2.

257 General solutions for the landslide velocities evolving as functions of time and position down the entire flow
 258 path, from initiation to the propagation, through the track to the run-out and final deposition, are obtained
 259 by combining the accelerating solutions (18)-(19) and the decelerating solutions (21)-(22).



260 5 Results

261 In order to illustrate the performances of our novel unified exact analytical solutions, below, I present results
262 for different scenarios and physical parameters representing real situations (Pudasaini and Krautblatter, 2022).
263 We can properly choose the slope angle, solid and fluid densities, the solid volume fraction, basal friction angle
264 of the solid, earth pressure coefficient, and the free-surface gradient such that α^a can be as high as 7, α_d can be
265 as high as 2, and β can be between 0.01 and 0.0025. In what follows, without loss of generality, the parameter
266 values for α^a , α_d and β are chosen from these domains. However, other values of these physical and model
267 parameters are possible within their admissible domains.

268 Landslide deceleration begins as the resisting forces overtake the driving forces. Analytical solutions reveal
269 that the mechanism and process of acceleration and deceleration, and the halting are fundamentally different.
270 This is indicated by the fact that the solutions to the accelerating system (1) appear in the form of the tangent
271 hyperbolic functions with the upper or lower limits (depending on the initial condition), whereas the solutions
272 for the decelerating system (2) appear to be in a special form of a decreasing tangent functions without bounds
273 for which the lower bounds should be set practically, typically the velocity is zero as the mass halts.

274 5.1 Simple solutions

275 I begin analyzing the performances of the landslide models and their exact analytical solutions for the most
276 simple situations where the motions can either be time-independent, or there is no internal deformation.
277 Solutions will be presented and discussed for the decelerating motions, and the combination of accelerating and
278 decelerating motions, and depositions.

279 5.1.1 Landslide deceleration

280 Landslide velocities in accelerating channels have been exclusively presented by Pudasaini and Krautblatter
281 (2022). Here, I consider solutions in decelerating portion of the channel as well as the mass halting. It might
282 be difficult to obtain initial velocity in the rapidly accelerating section in steep slope. But, in the lower portion
283 of the track, where where motion switches from accelerating to decelerating state, one could relatively easily
284 obtain the initial velocity that can be used further for dynamic computations. A simple situation arises when
285 the landslide enters the transition zone, and to the fan region such that the initial velocity could be measured
286 relatively easily at the fan mouth. Then, this information can be used to simulate the landslide velocity in the
287 run-out zone, its travel time, and the run-out length in the fan area. Figure 1 shows results for decelerating
288 motions. Once the landslide begins to decelerate (here, due to the negative net driving force), it decelerates
289 faster in time than in space, means the (negative) time gradient of the velocity is higher than its (negative)
290 spatial gradient. However, as it is closer to the deposition, the velocity decreases relatively smoothly in time.
291 But, its spatial decrease is rather abrupt. The travel or run-out time and distance are determined by setting
292 the deceleration velocity to zero in the solutions obtained for (4). We can consistently take initial time and
293 location down the slope such that the previously accelerating mass now begins to decelerate. As the travel time
294 and travel distance are directly connected by a function, we can uniquely determine the time and position at
295 the instance the motion changes from accelerating to decelerating state. At this occasion, the solution switches
296 from model (3) to model (4). In Fig. 1, I have suitably chosen the time and spatial boundaries (or initial
297 conditions) as $x = 1500$ m corresponding to $t = 50$ s for $u_0 = 50$ ms⁻¹.

298 This analysis provides us with basic understanding of the decelerating motion and deposition process in the
299 run-out region. I have analytically quantified the deceleration and deposition. The important observation from
300 Fig. 1 is that the time and spatial perspectives of the landslide deceleration and deposition are fundamentally
301 different. These are the manifestations of the inertial terms $\partial u/\partial t$ and $u\partial u/\partial x$ in the simple mass point and
302 steady-state landslide velocity models (7) and (8), and (3) and (4), respectively.

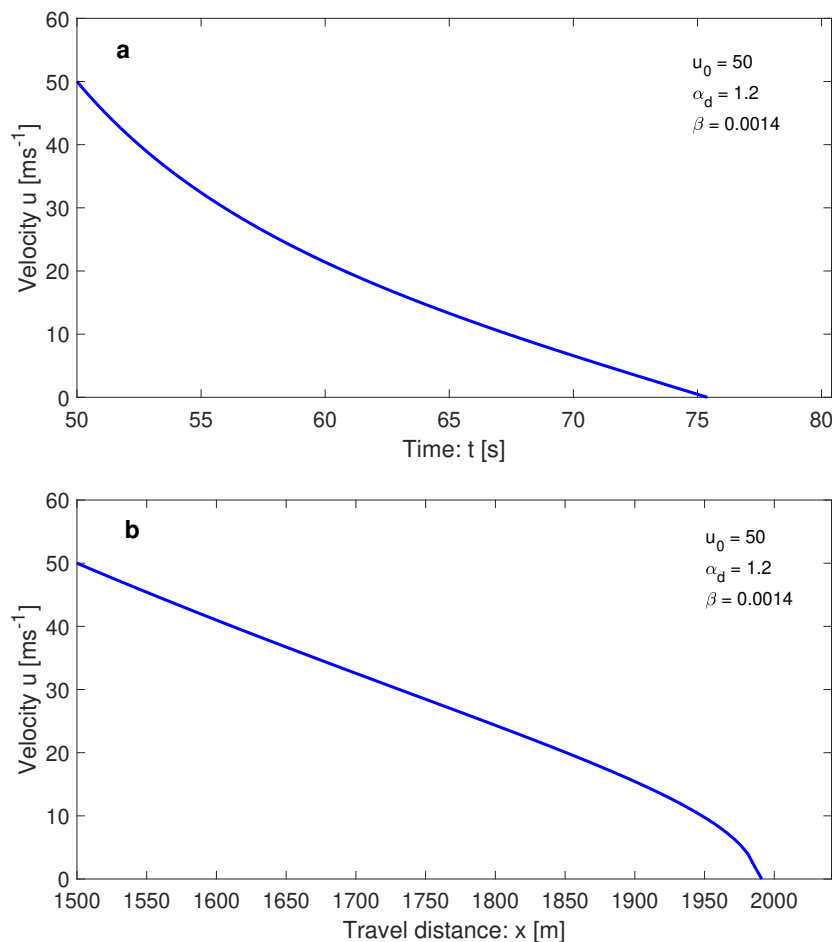


Figure 1: The landslide deceleration in time (a) and space (b) showing different dynamics for given physical parameters.

303 5.1.2 Landslide release and acceleration, deceleration and deposition: a transition

304 However, the above description is only one side of the total motion that must be unified with the solution in
305 the accelerating sector, and continuously connect them to automatically generate the whole solution. For a
306 rapid assessment of the landslide motion, technically the entire track can be divided into two major sectors,
307 the ascending sector where the landslide accelerates, followed by the descending sector where it decelerates
308 and finally comes to a halt. Assuming these approximations are practically admissible, this already drastically
309 reduces the complexity and allows us to provide a quick solution. To achieve this, here, I combine both the
310 solutions in the accelerating and decelerating portions of the channel. The process of landslide release and
311 acceleration, and deceleration and deposition are presented in Fig. 2 in two segments (sectors), for ascending
312 ($\alpha^a = 3.5$) and descending ($\alpha_d = 1.2$) sections, respectively. The initial value (left boundary) of the downstream
313 decelerating segment is provided by the final value (right boundary) of the upstream accelerating segment.
314 There are two key messages here. First, there are fundamental differences between the landslide release and
315 acceleration, and deceleration and deposition in space and time. In space, the changes in velocity are rapid at
316 the beginning of the mass release and acceleration and at the end of deceleration and deposition. However, in
317 time, these processes (changes in velocity) are relatively gentle at the beginning of mass release and acceleration,

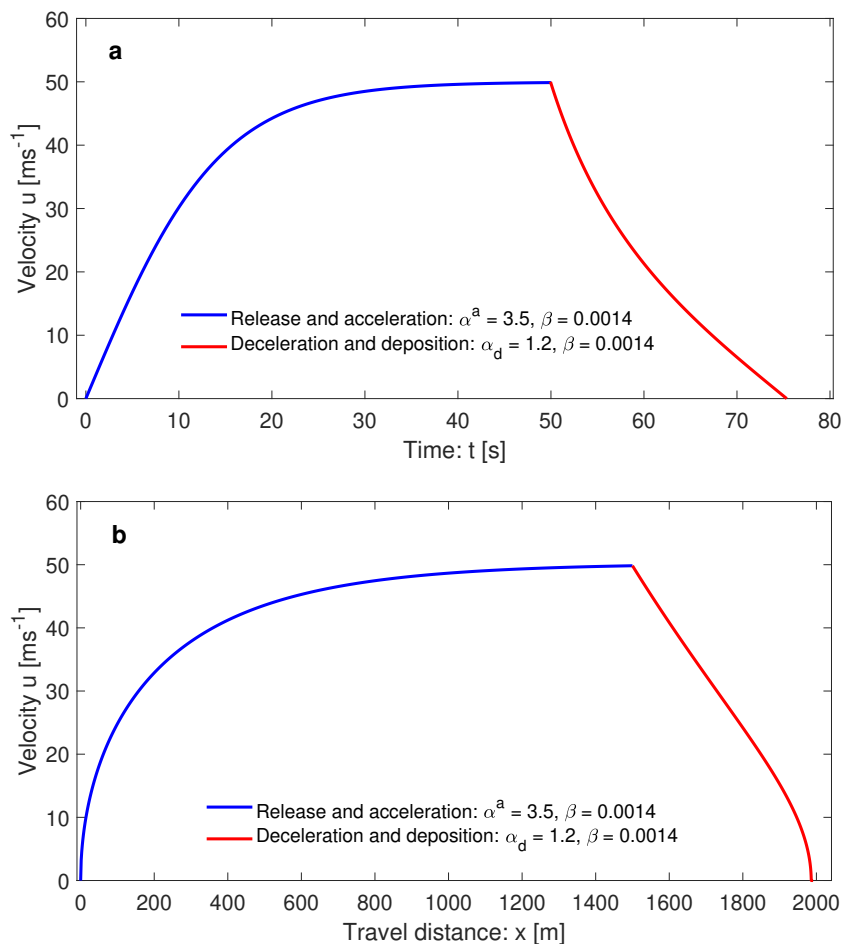


Figure 2: The landslide release and acceleration (left segments), deceleration and deposition (right segments) in time (a), and space (b) with chosen physical parameters. Also seen is the transition from acceleration to deceleration at kinks at about (50, 50) and (1500, 50), respectively. The landslide velocity dynamics are fundamentally different in time and space.

318 and at the end of deceleration and deposition. This means, the spatial and time perspectives of changes of
319 velocities are different. Second, the transition from acceleration to deceleration is of major interest, as this
320 changes the state of motion from driving force dominance to resisting force dominance, here, due to the negative
321 net driving force. The transition is more dramatic in time than in space. This manifests that the three critical
322 regions; release, transition from acceleration to deceleration, and deposition; must be handled carefully as they
323 provide very important information for the practitioners and hazard assessment professionals on the dynamics
324 of landslide motion, behavioral changes in different states and depositions. This means, the initial velocity, the
325 change in velocity from the accelerating to decelerating section, and the velocity close to the deposition must
326 be understood and modelled properly.



327 5.1.3 Landslide release and acceleration, deceleration and deposition: 328 multi-sectional transitions

329 The situations described above are only some rough approximations of reality as the landslide acceleration and
330 deceleration may often change locally, requiring to break its analysis in multiple sectors to more realistically
331 model the dynamics in greater details and higher accuracy to the observed data. In general, the landslide
332 moves down a variable track. For practical purpose, such a track can be realistically divided in to a multi-
333 sectional track (Dietrich and Krautblatter, 2019) such that at each section we can apply our analytical velocity
334 solutions, both for accelerating (sufficiently positive net driving force in relation of the initial velocity, or the
335 viscous drag force) and decelerating (negative net driving force) sections. The transitions between these sections
336 automatically satisfy the boundary conditions: The left boundary (initial value) of the following segment is
337 provided by the right boundary (final value) that is known from the analytical solution constructed in the
338 previous time, or space of the preceding segment. This procedure continues as far as the two adjacent segments
339 are joined, connecting either ascending–ascending, ascending–descending, or descending–descending velocity
340 segments. However, note that, independent of the number of segments and their connections, only one initial
341 (or boundary) value is required at the uppermost position of the channel. All other consecutive (internal and
342 final) boundary conditions will be systematically generated by our analytical solution system, derived and
343 explained at Section 3.

344 An ascending–ascending segment connection is formed when two ascending segments with different positive
345 net driving forces (larger than the drag forces) are connected together. A typical example is the connection
346 between a relatively slowly accelerating to a highly accelerating section. An ascending–descending segment
347 connection is constituted when an upstream ascending segment is connected with a downstream descending
348 segment, typically the connection between an accelerating to descending section. A descending–descending
349 segment connection is developed when the two descending segments with different negative net driving forces are
350 connected together. A typical example is the connection between a slowly decelerating to a highly decelerating
351 section. However, many other combinations between ascending and descending segments can be formed as
352 guided by the changes in the net driving forces, or the changes in the slope-induced and friction-induced forces
353 and their dominances. So, we need to extend the solution procedure of Section 5.1.2 from two sectoral landslide
354 transition to multi-sectoral transitions.

355 Figure 3 presents a typical (positive rate of ascendant, and negative rate of descendant) example of the multi-
356 sectoral solutions for the time evolution of the velocity field for the ascending ($\alpha^a = 4.0, 5.0, 6.0$), and the
357 descending ($\alpha_d = 0.15, 1.25, 1.90$) sectors, respectively. However, note that the α values on the ascending and
358 descending sectors are relative to each other. So, α_d on the descending sectors should be perceived as relatively
359 negative to α^a in the ascending sector. In the ascending sectors, as the net driving force increases, from the
360 first to the second to the third sector, the mass further accelerates, enhancing the slope of the velocity field
361 at each successive kink connecting the two neighboring segments. At the major kink, as the net driving force
362 changes rapidly from accelerating to decelerating mode with the value of $\alpha^a = 6.0$ to $\alpha_d = 0.15$, the motion
363 switches dramatically from the velocity ascending to descending state. In the following descending sectors, as
364 the values of α_d quickly increases, the mass further decelerates, from the fourth to the fifth to the sixth sector,
365 negatively reducing the slope of the velocity field at each successive kink, preparing for deposition. Finally,
366 the mass comes to a halt ($u = 0$) at $t = 50$ s. So, Fig. 3 reveals important time dynamics of ever-increasing
367 multi-sectoral ascending motions, its quick transition to descending motion, and the following ever-decreasing
368 descending motions, and the final mass halting. The main observation is the analytical quantification of the
369 complex dynamics of the landslide with increasing and decreasing gradients of the positive and negative net
370 driving forces. This can be a scenario for a track with multi-sectors of ever increasing slope, followed by a
371 quick transition to a decreasing slope, again succeeded by multi-sectors of ever decreasing slopes, and finally
372 mass deposition.

373 As the time and spatial perspectives of the landslide motions are different, and from the practical point of
374 view, it is even more important to acquire the velocity as a function of the channel position, next, I present
375 results for multi-sectoral landslide dynamics as a function of the channel position. Depending on the rates of
376 ascendance and descendance, I analyze the landslide dynamics separately. Figure 4 displays the results for the

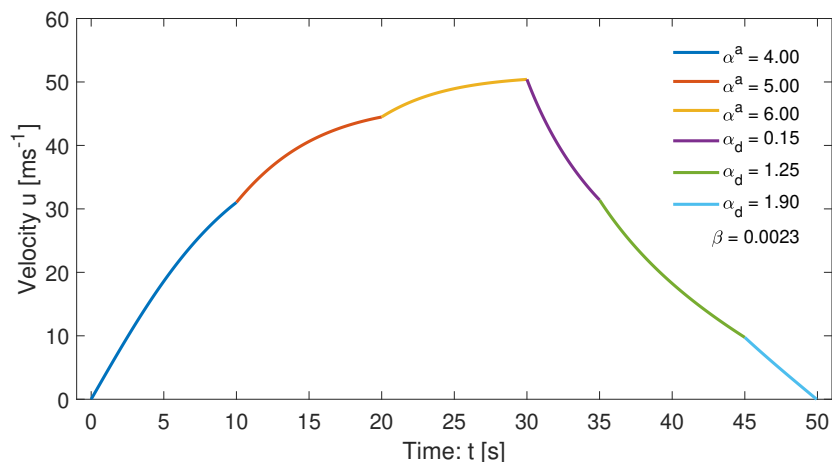


Figure 3: Landslide release and multi-sectional acceleration, deceleration and deposition in time. The physical parameters are shown in the legend. Several ascending–ascending and descending–descending segments are connected on the left with kinks at (10, 31.02) and (20, 44.48), and on the right with kinks at (35, 31.40) and (45, 9.75). The left and right segments are further connected by a central ascending–descending segment connection at the major kink at (30, 50.41). The mass stops at (50, 0.0).

377 evolution of the velocity field as a function of the travel distance as the landslide moves down the slope. To
 378 investigate the influence of the intensity of accelerating and decelerating net driving forces, two distinct sets
 379 of net driving forces are considered. In Fig. 4a, as the net driving force increases from the first to second
 380 to the third sectors, the acceleration increases, and the slopes of the velocity curves increase accordingly at
 381 kinks in these sectors. But, as the net driving force decreases from the third to fourth to the fifth sectors, the
 382 acceleration decreases although the landmass is still accelerating. In this situation, the velocity curves increase
 383 accordingly in these sectors, but slowly, and finally reach the maximum value. At the major kink, the net
 384 driving force has dropped quickly from $\alpha^a = 3.06$ to its decelerating value of $\alpha_d = 0.5$. Consequently, the
 385 motion switches dramatically from the velocity ascending (accelerating) to descending (decelerating) state. In
 386 the velocity descending sectors, as the values of α_d quickly increases, the mass further decelerates, but now
 387 much quicker than before, resulting in the negatively increased slope of the velocity fields at each successive
 388 kink. As controlled by the net decelerating force, α_d , the deposition process turned out to be rapid. Finally,
 389 the mass comes to a halt ($u = 0$) at $x = 1494$ m.

390 In Fig. 4b, the net driving driving force in the first sector is much higher than that in Fig. 4a. However,
 391 then, even in the ascending sectors, the net driving forces are steadily decreasing, resulting in the continuously
 392 decreased slopes of the velocity fields from the first to the fifth sectors. As in Fig. 4a, at the major kink, the
 393 net driving force dropped quickly from $\alpha^a = 3.79$ to its decelerating value of $\alpha_d = 0.5$, forcing the motion to
 394 switch dramatically from the velocity ascending to descending state. In the velocity descending sectors, as the
 395 values of α_d further increases, the mass decelerates steadily, faster than before, with the negatively increased
 396 slope of the velocity fields at each following kink. Due to the similar decelerating net driving forces as in Fig.
 397 4a, the deposition process turned out to be quite quick. Finally, the mass halts ($u = 0$) at $x = 1435$ m, a bit
 398 earlier than in Fig. 4a. So, Fig. 4 manifests that the slopes and connection appearances of the velocity fields
 399 exclusively depend on the boundary values and the net driving forces of the following sections.

400 The run-out distances in Fig. 4a and Fig 4b are similar. However, their internal dynamics are substantially
 401 different, here, mainly in the ascending sectors. The main essence here is that one cannot understand the
 402 overall dynamics of the landslide by just looking at the final deposit and the run-out length as in empirical and
 403 statistical models. Instead, one must also understand the entire and the internal dynamics in order to properly

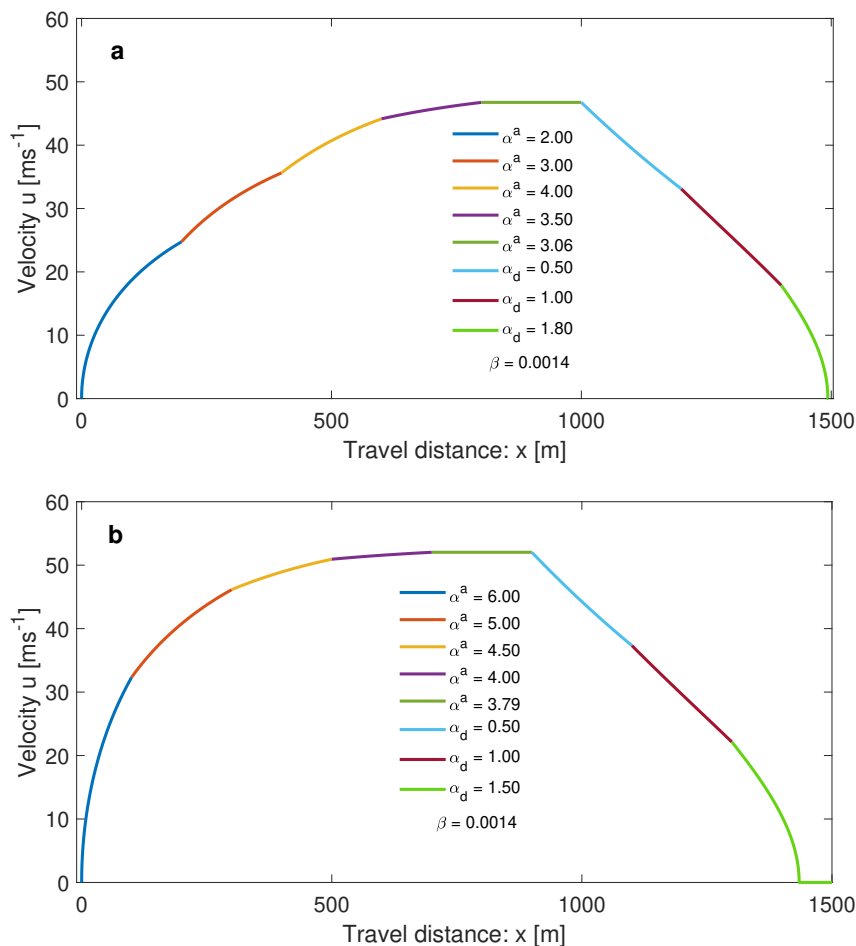


Figure 4: Landslide release and multi-sectional acceleration, deceleration and deposition in space with different parameter sets shown in the legends. **(a)** Several ascending–ascending segments are connected on the left with kinks at (200, 24.75), (400, 35.62), (600, 44.20), and (800, 46.75), and descending–descending segments are connected on right with kinks at (1200, 33.10), and (1400, 17.90). The left and right segments are further connected by a central ascending–descending segment connection at the major kink at (1000, 46.80). The landslide comes to a halt at (1494, 0.0). **(b)** Similarly, several ascending–ascending segments are connected on the left with kinks at (100, 32.35), (300, 46.14), (500, 50.94), and (700, 52.03), and descending–descending segments are connected on the right with kinks at (1100, 37.30), and (1300, 22.10). The left and right segments are further connected by a central ascending–descending segment connection at the major kink at (900, 52.03). The landslide comes to a halt at (1435, 0.0). Although **(a)** and **(b)** have similar run-out distances, their internal dynamics are different, so are the associated impact forces along the tracks.

404 simulate the motion and the associated impact force. So, our physics-based complete analytical solutions
 405 provide much better descriptions of landslide dynamics than the angle of reach based empirical or statistical
 406 models (Heim, 1932; Lied and Bakkehøi, 1980) that explicitly rely on parameter fits (Pudasaini and Hutter,
 407 2007).

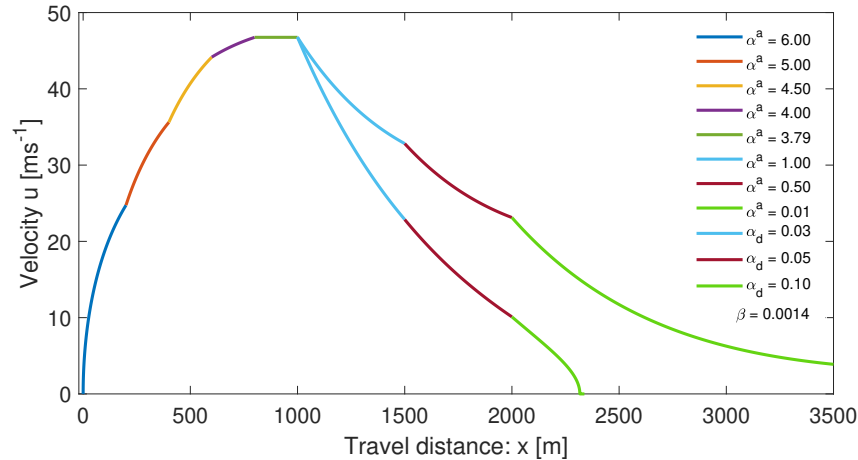


Figure 5: Landslide release and multi-sectional acceleration, deceleration and deposition in space with different physical parameters sets shown in the legend. Two different decelerating motions are considered for the right sectors. The upper velocities on the right are produced with the solution of the model (1) with positive net driving forces producing kinks at (1500, 32.82) and (2000, 23.12), whereas the lower velocities on the right are produced with the solution of the model (2) with negative net driving forces producing kinks as (1500, 22.87) and (2000, 10.10), respectively. The corresponding descending motions in the common track domains are displayed with the same color-codes. Their dynamics and deposition processes are quite different. The negative net driving forces result in the realistic deceleration, run-out and deposition at (2317, 0), while even after travelling 3500 m, the decelerating motion with positive net driving forces still has high velocity (3.88 ms^{-1}), and cannot represent reality.

5.1.4 Decelerating landslide with positive and negative net driving forces

The previously accelerating landslide may transit to decelerating motion such that the net driving force α^a is positive in both sections, but α^a is smaller in the succeeding section, i.e., $\alpha_p^a > \alpha_s^a$, where, p and s indicate the preceding and succeeding sections. Assume that the end velocity of the preceding section is u_p . Then, if $u_p > \sqrt{\alpha_s^a/\beta}$, the landslide will decelerate in the succeeding section such that the velocity in this section is bounded from below by $\sqrt{\alpha_s^a/\beta}$. This can happen when the slope decreases and/or friction increases, but, still, the net driving force remains positive. However, as the initial velocity of the succeeding section is higher than the characteristic limit velocity of this section, $\sqrt{\alpha_s^a/\beta}$, the velocity must decrease as it is controlled by the resisting force, namely the drag. If the slope is quite long with this state, the landslide velocity will approach $\sqrt{\alpha_s^a/\beta}$, and then, continue almost unchanged. A particular situation is the vanishing net driving force, i.e., $\alpha_s^a = 0$, in the right section. This can prevail when the gravity and frictional forces balance each other. Then, as the landslide started with the positive (high) velocity in the left boundary of the right section, it is continuously resisted by the drag force, strongly at the beginning, and slowly afterwards, as the velocity decreases substantially. If the channel is sufficiently long (and $\alpha_s^a = 0$), then the drag can ultimately bring the landslide velocity down to zero. Yet, this is a less likely scenario to take place in nature. In all these situations, which are associated with the positive net driving forces, we must consistently use the model (1) and its corresponding analytical solutions. In another scenario, assume that the landslide transits to the next section where it experiences the negative net driving force. Then, in this section, we must use the model (2) and its corresponding analytical solutions.

Figure 5 presents the first rapidly accelerating motions in the left sections, as in Fig. 4a, followed by decelerating motions in the right sections. However, as the mass transits to the right sections at $x = 1000$, there can be fundamentally two types of decelerating motions. (i) The motions can still be associated with the positive net



430 driving forces. Or, (ii) the motions must be associated with the negative net driving forces. This depends
431 on the actual physical situation, and either (i) or (ii) can be true. The lower velocities on the right are
432 produced with the solution of the model (2) with negative net driving forces, whereas the upper velocities
433 are produced with the solution of the model (1) with positive net driving forces. For better visualization,
434 and ease of comparison, the domain of decelerating motion and deposition has been substantially enlarged.
435 The important point is that, the two solutions on the right show completely different dynamics. On the one
436 hand, the decelerating solutions represented by the upper curves on the right are less realistic as these take
437 unrealistically long time until the mass comes to stop, and the velocities are also unreasonably high. On the
438 other hand, such solutions can mainly be applied for the relatively low positive net driving forces and high
439 initial velocities. However, the lower curves on the right are realistic, and are produced by using the solutions
440 for the naturally decelerating motions associated with the negative net driving forces, as is the case in natural
441 setting. For the solutions described by the negative net driving forces, the mass deceleration is fast, velocity
442 is low, close to the flow halting the velocity drops quickly to zero, and the landslide stops realistically as
443 expected. Figure 5 is of practical importance as it clearly reveals the fact that we must appropriately model
444 the descending landslide motions. The important message here is that the descending and deposition processes
445 of a landslide must be described by the decelerating solutions with negative net driving forces (the solutions
446 derived here), but not with the decelerating solutions described by positive net driving forces (the solutions
447 derived in Pudasaini and Krautblatter, 2022). So, Fig. 5 has strong implications in real applications that the
448 new set of analytical solutions with negative net driving forces must be appropriately considered in describing
449 the descending landslide motion.

450 5.2 Time and spatial evolution of landslide velocity: general solutions

451 The solutions presented in Section 5.1 only provide information of the landslide dynamics either in time or in
452 space, but not the both. As the landslide moves down the slope, in general, its velocity evolves as a function of
453 time and space. Pudasaini and Krautblatter (2022) presented the time marching of the landslide motion that
454 also stretches as it accelerates downslope. Such deformation of the landslide stems from the advection, $u\partial u/\partial x$,
455 and the applied forces, $\alpha^a - \beta u^2$. The mechanism of landslide advection, stretching and the velocity up-lifting
456 has been explained. They revealed the fact that shifting, up-lifting and stretching of the velocity field emanate
457 from the forcing and non-linear advection. The intrinsic mechanism of their solution describes the breaking
458 wave and emergence of landslide folding. This happens collectively as the solution system simultaneously
459 introduces downslope propagation of the domain, velocity up-lift and non-linear advection. Pudasaini and
460 Krautblatter (2022) disclosed that the domain translation and stretching solely depends on the net driving
461 force, and along with advection, the viscous drag fully controls the shock wave generation, wave breaking,
462 folding, and also the velocity magnitude.

463 Pudasaini and Krautblatter (2022) considered the accelerating motion. Assuming that the landslide has already
464 propagated a sufficient distance downslope, here, I focus on time and spatial evolution of landslide velocity for
465 the decelerating motion and deposition for which I apply the new solutions given by (21)-(22). This complements
466 the existing solutions and presents the unified analytical description of the landslide motion down the entire
467 slope. So, next I present more general results for landslide velocity for decelerating motion controlled by the
468 advection, $u\partial u/\partial x$, and the applied forces, $-\alpha_d - \beta u^2$. In contrast to the accelerating motion, the decelerating
469 motion is associated with the applied force $-\alpha_d - \beta u^2$, while the structure of the advection, $u\partial u/\partial x$, remains
470 unchanged. Now, the landslide may be stretched or compressed, however, the velocity will gradually sink. The
471 intensity of the wave breaking and the landslide folding will be reduced. This happens, because the solution
472 system introduces downslope propagation of the domain, velocity sink and non-linear advection. Moreover, the
473 domain translation and stretching or contracting depends on the net driving force, and paired with advection,
474 the viscous drag controls the shock wave generation, wave breaking, folding, and also the reduction of the
475 velocity magnitude.

476 From the geomorphological, engineering, planning and hazard mitigation point of view, the deposition and run-
477 out processes are probably the most important aspects of the landslide dynamics. So, in this section, I focus
478 on the dynamics of the landslide as it decelerates and enters the run-out area and the process of deposition,

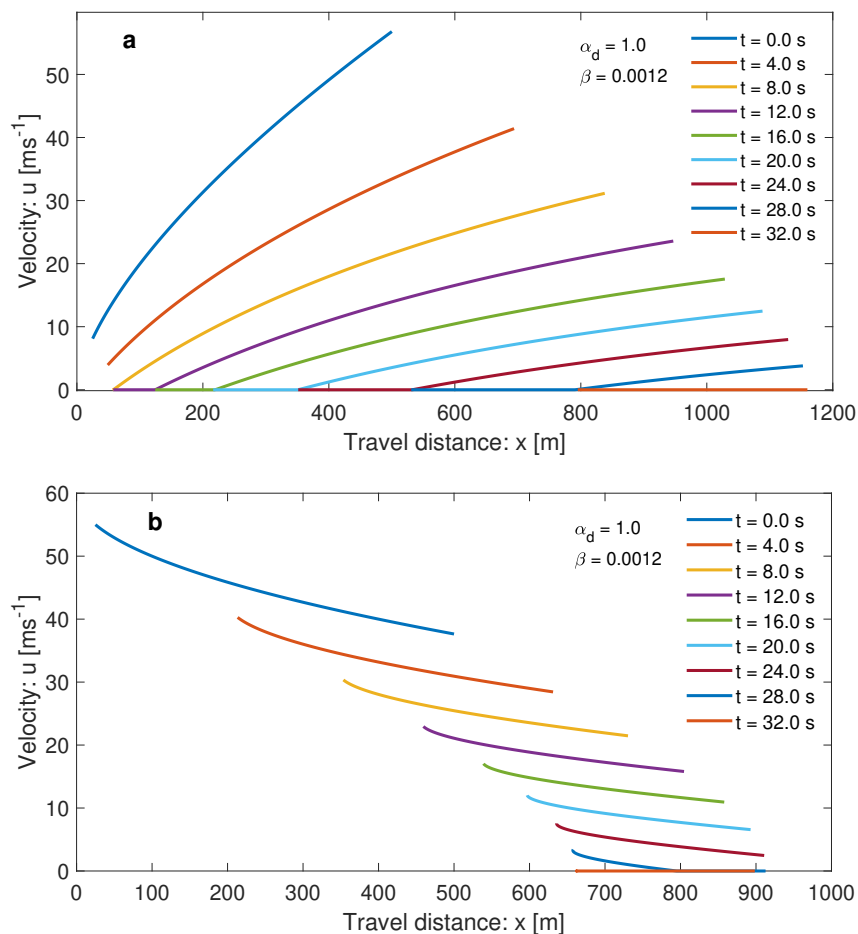


Figure 6: Time and spatial evolution of the landslide velocity showing the motion, deformation and deposition of initially ascending (a), and descending (b) landslide fronts, described by $s_0(x) = x^{0.65}$ and $s_0(x) = 60 - x^{0.5}$, respectively, at $t = 0$ s. The physical parameter values are shown. The initially different velocity profiles result in completely different travel distances and landslide spreadings or contractings. The deposition extend for the ascending front is much longer than the same for the descending front.

479 including its stretching or contracting behavior.

480 5.2.1 Landslide depositions of initially ascending and descending fronts

481 In the most simple situation, the landslide may start deceleration and enter the run-out and the fan zone
 482 with either the ascending or descending front. An ascending front may represent the pre-mature transition,
 483 while a descending front may signal the mature transition to the run-out zone. Figure 6 describes the prop-
 484 agation dynamics and deposition processes for initially ascending (a) and descending (b) fronts. The initial
 485 velocity distributions are chosen following Pudasaini and Krautblatter (2022). In Fig. 6a, the front decelerates
 486 much faster than the rear, while in Fig. 6b, it is the opposite. This leads to the forward propagating and
 487 elongating landslide mass for the ascending front while forward propagating and compressing landslide mass
 488 for the descending front. This results in completely different travel distances and deposition processes. The
 489 runout distance is much longer in Fig. 6a than in Fig. 6b. The striking difference is observed in the lengths

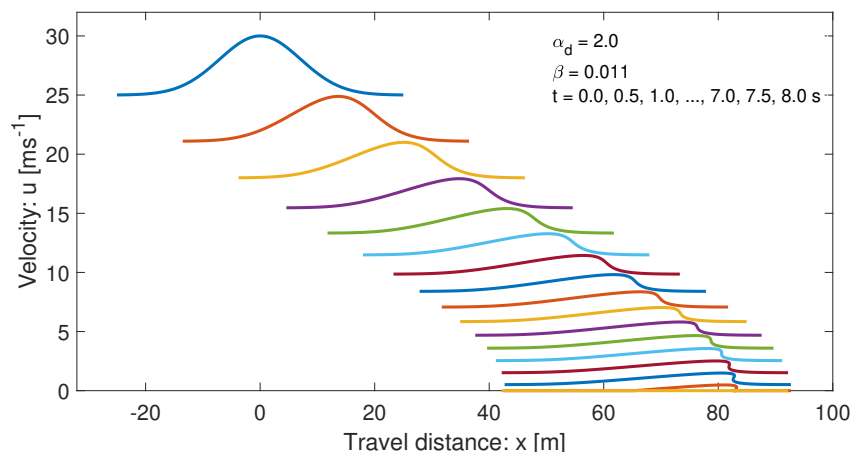


Figure 7: Time and space evolution of the propagating landslide and deposition waves. The initial velocity distribution is given by $s_0(x) = 5 \exp[-x^2/100] + 25$ at $t = 0$ s. The physical parameter values are shown.

490 of the deposited masses. The deposition extend for the ascending front is much longer (about 1100 m) than
491 the same for the descending front (which is < 250 m). At a first glance, it is astonishing. However, it can
492 be explained mechanically. Ascending or descending fronts lead to the strongly stretching and compressing
493 behavior, resulting, respectively, in the very elongated and compressed depositions of the landslide masses. In
494 Fig. 6a, although the front decelerates faster than the rear, the rear velocity drops to zero faster than the front,
495 whereas the velocity of the front becomes zero at a later time. So, the halting process begins much earlier, first
496 from the rear and propagates to the front that takes quite a while. This results in the remarkable stretching of
497 the landslide. Nevertheless, in Fig. 6b, although the rear decelerates faster than the front, the front velocity
498 quickly drops to zero much faster than the rear, whereas the velocity of the rear becomes zero at a much
499 later time. So, the halting process begins first from the front and propagates to the rear that takes quite a
500 while. This results in the remarkable compression of the landslide. This demonstrates how the different initial
501 velocity profiles of the landslides result in completely different travel distances and spreadings or contractings
502 in depositions.

503 The state of deposition is important in properly understanding the at-rest-structure of the landmass for geomor-
504 phological and civil or environmental engineering considerations. Energy dissipation structures, e.g., breaking
505 mounds, can be installed in the transition and the run-out zones to substantially reduce the landslide velocity
506 (Pudasaini and Hutter, 2007; Johannesson et al., 2009). Here comes the direct application of our analytical
507 solution method. The important message here is that, if we can control the ascending frontal velocity of the
508 landslide and turn it into a descending front, by some means of the structural measure in the transition or the
509 run-out zone, we might increase compaction and control the run-out length. This will have a immediate and
510 great engineering and planning implications, due to increased compaction of the deposited material and the
511 largely controlled travel distance and deposition length.

512 5.2.2 Landslide deposition waves

513 The situation discussed in the preceding section only considers a monotonically increasing or a monotonically
514 decreasing velocity front in the transition or run-out (fan) zones. However, in reality, the landslide may enter
515 transition or the fan zone with a complex wave form, representative of a surge wave. A more general situation
516 is depicted in Fig. 7 which continuously combines the ascending and descending parts in Fig. 6, but also
517 includes upstream and downstream constant portions of the landslide velocities thus, forming a wave structure.
518 The initial velocity distribution is chosen following Pudasaini and Krautblatter (2022). As the frontal and

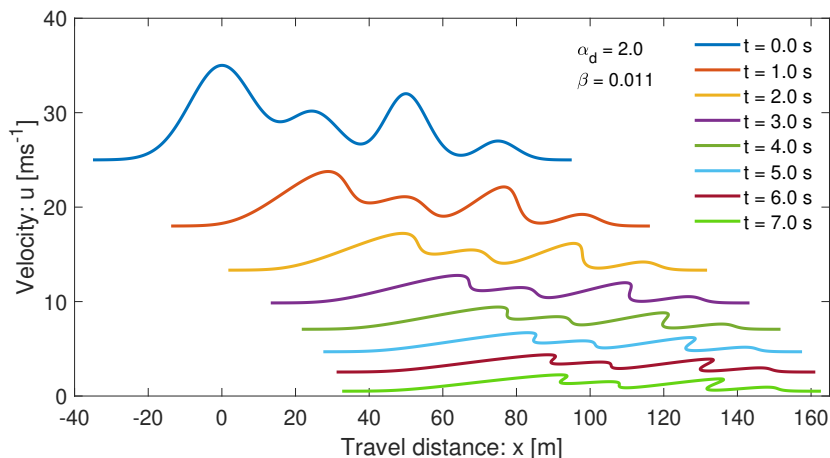


Figure 8: Time and space evolution of the landslide with multiple complex waves, foldings and crests during the propagation and deposition processes. The initial velocity distribution ($t = 0$ s) is given by the function $s_0(x) = 10 \exp[-(x - 0)^2 / 150] + 5 \exp[-(x - 25)^2 / 100] + 7 \exp[-(x - 50)^2 / 65] + 2 \exp[-(x - 75)^2 / 50] + 25$. The chosen physical parameter values are shown in the legend.

519 the rear portions of the landslide initially have constant velocities, due to its initial velocity distribution with
520 maximum in between, it produces a pleasing propagation mosaic and the final settlement. Because, now, both
521 the front and the rear decelerate at the same rates, deposition begins from both sides. Although, in total, the
522 landslide elongates (but not that much), it mainly elongates in the rear side while compressing a bit in the
523 frontal portion. The velocity becomes smoother in the back side of the main peak while it tends to produce a
524 kink in the frontal region. This forces to generate a folding in the frontal part which is seen closer to the halting.
525 However, the folding is controlled by the relatively high applied drag. If the applied drag would have been
526 substantially reduced, dominant folding would have been observed. Note that, the folding of the accelerating
527 landslide has been covered in Pudasaini and Krautblatter (2022). The important idea here is that, the folding
528 and the wave that may be present in the frontal part of the landslide evolution or deposition, can be quantified
529 and described by our general exact analytical solution.

530 5.2.3 Landslide with multiple waves, foldings, crests and deposition pattern

531 The landslide may descend down and enter the transition and the run-out zone with multiple surges of different
532 strengths, as frequently observed in natural events. In reality, the initial velocity can be even more complex
533 than the one utilized in Fig. 7. To describe such situation, Fig. 8 considers a more general initial velocity
534 distribution than before with multiple peaks and troughs of different strengths and extents represented by a
535 complex function. As the landslide moves down, it produces a beautiful propagation pattern with different
536 stretchings and contractings resulting in multiple waves, foldings, crests and deposition. Depending on the
537 initial local velocity distribution (on the left and right side of the peak), in some regions, strong foldings and
538 crests are developed (corresponding to the first and third initial peaks), while in other regions only weak folding
539 (corresponding to the second initial peak) is developed, or even the peak is diffused (corresponding to the fourth
540 initial peak). This provides us with the possibility of analytically describing complex multiple waves, foldings
541 and crests formations during the landslide motion and also in deposition. This analysis can provide us with
542 crucial information of a complex deposition pattern that can be essential for the study of the geomorphology
543 of deposit. Importantly, the local information of the degree of compaction and folding can play a vital role in
544 landuse planning, and decision making, e.g., for the choice of the location for the infrastructural development.

545 Technically, the results presented in Fig. 2 to Fig. 8 demonstrate that, computationally costly simulations may



546 now be replaced by a simple highly cost-effective, clean and honourable analytical solutions (almost without
547 any cost). This is a great advantage as it provides immediate and very easy solution to the complex landslide
548 motion once we know the track geometry and the material parameters, which, in general, is known from the
549 field. So, we have presented a seminal technique describing the entire landslide motion and deposition process.

550 6 Summary

551 I have constructed several new exact analytical solutions and combined these with the existing solutions for
552 the landslide velocity. This facilitated the unified description of a landslide down a slope with multiple seg-
553 ments with accelerating and decelerating movements as well as the landslide run-out, and deposition. This
554 provided the complete and righteous depiction of the landslide motions in different segments, for the entire
555 slope, from its release, through the track until it comes to a standstill. Our analytical method couples sev-
556 eral ascending–ascending, ascending–descending, or descending–descending segments to construct the exact
557 multi-sectoral velocity solutions down the entire track. I have analytically quantified the complicated landslide
558 dynamics with increasing and decreasing gradients of the positive and negative net driving forces. The impli-
559 cation is: the new set of analytical solutions with negative net driving forces must be appropriately considered
560 in real applications in describing the descending landslide motion as such solutions better represent the natural
561 process of decreasing motion and deposition. Analytical solutions revealed essentially different novel mecha-
562 nisms and processes of acceleration and deceleration and the mass halting. There are fundamental differences
563 between the landslide release and acceleration, and deceleration and deposition in space and time. The tran-
564 sition from acceleration to deceleration takes place with strong kinks that changes the state of motion from a
565 primarily driving force dominance to resisting force dominance region. This manifests the three critical regions;
566 release, transition from acceleration to deceleration, and deposition; that must be handled carefully. The time
567 and spatial perspectives of the landslide deceleration and deposition appeared to be fundamentally different as
568 the transition is more dramatic in time than in space. We can uniquely ascertain the exact time and position
569 at the instance the motion changes from accelerating to decelerating state. Considering all the ascending and
570 descending motions, we can analytically obtain the exact total travel time and the travel distance for the whole
571 motion. These quantities are of direct practical importance as they supply us with all the necessary information
572 to fully describe the landslide dynamics.

573 Our physics-based complete, general analytical solutions disclose a number of important information for the
574 practitioners and hazard assessment professionals on the vitally important physics of landslide motion and
575 settlement. Essentially, these solutions provide much better overall descriptions of landslide dynamics than
576 the empirical or statistical models, which explicitly rely on parameter fits, but can only deal with the run-out
577 length. Our models provide information on the entire and internal dynamics that is needed to properly simulate
578 the motion and associated impact force. Our solutions provide insights into the process of compaction, and
579 the mechanism to control the travel distance and deposition length. The frontal folding and the wave, that
580 may appear during the landslide evolution or deposition, can be quantified by our analytical solution. We
581 have demonstrated that different initial landslide velocity distributions result in completely dissimilar travel
582 distances, deposition processes, and spreadings or contractings. Ascending and descending fronts lead to the
583 strongly stretching and compressing behavior resulting, respectively, in the very elongated and shortened run-
584 outs. The striking difference is observed in the lengths of the deposited masses. Time and space evolution
585 of the marching landslide and deposition waves produce a beautiful pattern and the final settlement. Initial
586 velocity distribution with multiple peaks and troughs of different strengths and extents lead to a spectacular
587 propagation pattern with distinct stretchings and contractings resulting in multiple waves, foldings, crests and
588 depositions. Depending on the initial local velocity distribution, in some regions strong foldings and crests
589 are developed, while in other regions foldings and crests are diffused. This provides us with the possibility of
590 analytically describing complex multiple waves, foldings and crests formations during the landslide motion and
591 deposition. As complex multiple surges of varying strengths can be explained analytically, our method provides
592 us with crucial geomorphological information of the sophisticated deposition pattern, including the important
593 local state of compaction and folding, which play a vital role in landuse planning, and decision making for
594 the infrastructural development and environmental protection. Moreover, our analytical method demonstrates



595 that computationally costly solutions may now be replaced by a simple, highly cost-effective and unified ana-
596 lytical solutions (almost without any cost) down the entire track of the landslide. This is of a great technical
597 advantage for the landslide practitioners and engineers as it provides immediate and very easy solution to the
598 complex landslide motion.

599 Acknowledgements

600 I greatly appreciate the fruitful discussions with and suggestions from Jens Turowski that helped to substantially
601 improve the paper.

602 References

- 603 [1] Baselt, I., de Oliveira, G.Q., Fischer, J.-T., Pudasaini, S.P., 2021. Evolution of stony debris flows in laboratory
604 experiments. *Geomorphology* 372, 107431. <https://doi.org/10.1016/j.geomorph.2020.107431>.
- 605 [2] Berger, C., McArdell, B.W., Schlunegger, F., 2011. Direct measurement of channel erosion by debris flows, Illgraben,
606 Switzerland. *J. Geophys. Res. Earth Surf.* 116, F01002.
- 607 [3] Burgers, J.M., 1948. A mathematical model illustrating the theory of turbulence. In *Advances in Applied Mechanics*,
608 pp 171-199. Academic Press Inc., New York, edited by Richard von Mises and Theodore von Karman.
- 609 [4] Chalfen, M., Niemiec, A., 1986. Analytical and numerical solution of Saint-Venant equations. *Journal of Hydrology*
610 86(1-2), 1-13.
- 611 [5] Cuomo, S., Pastor, M., Capobianco, V., Cascini, L., 2016. Modelling the space time evolution of bed entrainment
612 for flow-like landslides. *Engineering Geology* 212, 10-20.
- 613 [6] de Haas, T., Nijland, W., de Jong, S.M., McArdell, B.W., 2020. How memory effects, check dams, and channel ge-
614 ometry control erosion and deposition by debris flows. *Scientific Reports*. 10, 14024. <https://doi.org/10.1038/s41598-020-71016-8>.
- 615 [7] de Haas, T., van Woerkom, T., 2016. Bed scour by debris flows: experimental investigation of effects of debris flow
616 composition. *Earth Surf. Process. Landforms* 41, 1951-1966.
- 617 [8] Dietrich, A., Krautblatter, M., 2019. Deciphering controls for debris-flow erosion derived from a LiDAR-recorded
618 extreme event and a calibrated numerical model (Rossbichelbach, Germany). *Earth Surf. Process. Landform* 44,
619 1346-1361.
- 620 [9] Dowling, C.A., Santi, P.M., 2014. Debris flows and their toll on human life: a global analysis of debris-flow fatalities
621 from 1950 to 2011. *Nat. Hazards* 71(1), 203-227.
- 622 [10] Evans, S.G., Bishop, N.F., Smoll, L.F., Murillo, P.V., Delaney, K.B., Oliver-Smith, A., 2009. A re-examination of
623 the mechanism and human impact of catastrophic mass flows originating on Nevado Huascarán, Cordillera Blanca,
624 Peru in 1962 and 1970. *Eng. Geol.* 108, 96-118.
- 625 [11] Faraoni, V., 2022. Helmholtz problem for the Riccati equation from an analogous Friedmann equation. *Eur. Phys. J.*
626 *C* 82. <https://doi.org/10.1140/eplc/s10052-021-09966-0>.
- 627 [12] Faug, T., Chanut, B., Beguin, R., Naaim, M., Thibert, E., Baraudi, D., 2010. A simple analytical model for pressure
628 on obstacles induced by snow avalanches. *Ann. Glaciol.* 51 (54), 1-8.
- 629 [13] Frank, F., McArdell, B.W., Huggel, C., Vieli, A., 2015. The importance of entrainment and bulking on debris flow
630 runout modeling: examples from the Swiss Alps. *Nat. Hazards Earth Syst. Sci.* 15, 2569-2583.
- 631 [14] Gauer, P., 2018. Considerations on scaling behavior in avalanche flow along cycloidal and parabolic tracks. *Cold Reg.*
632 *Sci. Technol.* 151, 34-36.
- 633 [15] Gubler, H., 1989. Comparison of three models of avalanche dynamics. *Annals of Glaciology* 13, 82-89.
- 634 [16] Heim, A., 1932. Bergsturz und menschenleben. *Geologische Nachlese* Nr. 30, Naturforschenden Gesellschaft in Zürich
635 77, 220.
- 636 [17] Iverson, R. M., Ouyang, C., 2015. Entrainment of bed material by earth-surface mass flows: review and reformulation
637 of depth-integrated theory. *Rev. Geophys.* 53(1), 27-58.
- 638



- 639 [18] Johannesson, T., Gauer, P., Issler, D., Lied, K., 2009. In: Barbolini, M., Domaas, U., Harbitz, C.B., Johannesson,
640 T., Gauer, P., Issler, D., Lied, K., Faug, T., Naaim, M. (Eds.), *The Design of Avalanche Protection Dams. Recent*
641 *Practical and Theoretical Developments*. European Commission. Directorate General for Research.
- 642 [19] Le, L., Pitman, E.B., 2009. A model for granular flows over an erodible surface. *SIAM J. Appl. Math.* 70, 1407-1427.
- 643 [20] Lied, K., Bakkehøi, S. 1980. Empirical calculations of snow-avalanche run-out distance based on topographic param-
644 eters. *Journal of Glaciology* V26, 165–178.
- 645 [21] Liu, W., Yang, Z., He, S., 2021. Modeling the landslide-generated debris flow from formation to propagation and
646 run-out by considering the effect of vegetation. *Landslides* 18, 43–58.
- 647 [22] McClung, D.M., 1983. Derivation of Voellmy's Maximum Speed and Run-Out Estimates from a Centre-of-Mass
648 Model. *Journal of Glaciology* 29(102), 350-352.
- 649 [23] McDougall, S., Hungr, O., 2005. Dynamic modelling of entrainment in rapid landslides. *Can. Geotech. J.* 42, 1437-
650 1448.
- 651 [24] Mergili, M., Jaboyedoff, M., Pullarello, J., Pudasaini, S.P., 2020. Back calculation of the 2017 Piz Cengalo - Bondo
652 landslide cascade with r.avaflow: what we can do and what we can learn. *Nat. Hazards Earth Syst. Sci.* 20, 505-520.
- 653 [25] Montecinos, G.I., 2015. Analytic solutions for the Burgers equation with source terms. arXiv:1503.09079v1.
- 654 [26] Perla, R., Cheng, T.T., McClung, D.M., 1980. A two-parameter model for snow-avalanche motion. *J. Glaciology*
655 26(94), 197-207.
- 656 [27] Pilvar, M., Pouraghniaei, M.J., Shakibaenia, A., 2019. Two-dimensional sub-aerial, submerged, and transitional
657 granular slides. *Physics of Fluids* 31, 113303. <https://doi.org/10.1063/1.5121881>.
- 658 [28] Pudasaini, S.P., Krautblatter, M., 2022. The landslide velocity. *Earth Surf. Dynam.* 10, 165–189,
659 <https://doi.org/10.5194/esurf-10-165-2022>, 2022.
- 660 [29] Pudasaini, S.P., Krautblatter, M., 2021. The mechanics of landslide mobility with erosion. *Nat. Commun.* 12, 6793,
661 <https://doi.org/10.1038/s41467-021-26959-5>, 2021.
- 662 [30] Pudasaini, S.P., Mergili, M., 2019. A multi-phase mass flow model. *Journal of Geophysical Research: Earth Surface*,
663 124, 2920-2942.
- 664 [31] Pudasaini, S.P., 2016. A novel description of fluid flow in porous and debris materials. *Eng. Geol.* 202, 62-73.
- 665 [32] Pudasaini, S.P., 2012. A general two-phase debris flow model. *J. Geophysics. Res.* 117, F03010.
666 [doi:10.1029/2011JF002186](https://doi.org/10.1029/2011JF002186).
- 667 [33] Pudasaini, S.P., Hutter, K., 2007. *Avalanche Dynamics: Dynamics of Rapid Flows of Dense Granular Avalanches*.
668 Springer, Berlin, New York.
- 669 [34] Salm, B., 1966. Contribution to avalanche dynamics. *International Symposium on Scientific Aspects of Snow and Ice*
670 *Avalanches, 1965, Davos*; pp. 199-214: IAHS Publ. No. 69.
- 671 [35] Shugar, D. H., Jacquemart, M., Shean, D., et al., 2021. A massive rock and ice avalanche caused the 2021 disaster at
672 Chamoli, Indian Himalaya. *Science* 373, 300–306.
- 673 [36] Theule, J.I., Liebault, F., Laigle, D., Loye, A., Jaboyedoff, M., 2015. Channel scour and fill by debris flows and
674 bedload transport. *Geomorphology* 243, 92-105.
- 675 [37] Voellmy, A., 1955. Über die Zerstörungskraft von Lawinen. *Schweizerische Bauzeitung. Jahrg. 73. Ht. 12.*, 159-162;
676 *Ht. 15*, 212-217; *Ht. 17*, 246-249; *Ht. 19*, 280-285. On the destructive force of avalanches, Translation No. 2. Alta.
677 *Avalanche Study Center, USDA, Forest Service, 1964.*